Title
A genetically encoded tool for manipulation of NADP+/NADPH in living cells

Journal
Nature Chemical Biology, 13(10)

ISSN
1552-4450

Authors
Cracan, Valentin
Titov, Denis V
Shen, Hongying
et al.

Publication Date
2017-10-01

DOI
10.1038/nchembio.2454

Peer reviewed

Published in final edited form as:

Nat Chem Biol. 2017 October ; 13(10): 1088–1095. doi:10.1038/nchembio.2454.

A genetically encoded tool for manipulation of NADP+/NADPH in living cells

Valentin Cracan[1,2,3,†], **Denis V. Titov**[1,2,3,†], **Hongying Shen**[1,2,3], **Zenon Grabarek**[1,*], and **Vamsi K. Mootha**[1,2,3,*]

[1]Howard Hughes Medical Institute and Department of Molecular Biology, Massachusetts General Hospital, Boston, MA, USA

[2]Department of Systems Biology, Harvard Medical School, Boston, MA, USA

[3]Broad Institute, Cambridge, MA, USA

Abstract

NADH and NADPH are redox coenzymes broadly required for energy metabolism, biosynthesis and detoxification. Despite detailed knowledge of specific enzymes and pathways that utilize these coenzymes, a holistic understanding of the regulation and compartmentalization of NADH and NADPH-dependent pathways is lacking, in part because of a lack of tools with which to investigate them in living cells. We previously reported the use of the naturally occurring *Lactobacillus brevis* H_2O-forming NADH oxidase (*Lb*NOX) as a genetic tool for manipulation of the NAD^+/NADH ratio in human cells. Here we present TPNOX (triphosphopyridine nucleotide oxidase), a rationally designed and engineered mutant of *Lb*NOX that is strictly specific towards NADPH. We characterize the effects of TPNOX expression on cellular metabolism and use it in combination with *Lb*NOX to show how the redox states of mitochondrial NADPH and NADH pools are connected.

Graphical Abstract

*Corresponding authors: Vamsi K. Mootha, M.D., vamsi@hms.harvard.edu, Zenon Grabarek, Ph.D., grabarek@molbio.mgh.harvard.edu, 185 Cambridge Street 6th Floor, Boston, MA 02114 USA.
†These authors contributed equally to this work

Author Contributions

VC, DVT, ZG and VKM designed the study and interpreted data. VC and ZG performed the biochemical and structure-related experiments. DVT, VC, and HS performed cell-based experiments. VC, DVT, ZG and VKM wrote the manuscript.

Data Availability Statement

Protein coordinates and structure factors for *Lb*NOX–NADH and TPNOX–NADPH have been submitted to the Protein Data Bank (PDB codes 5VN0 and 5VOH).

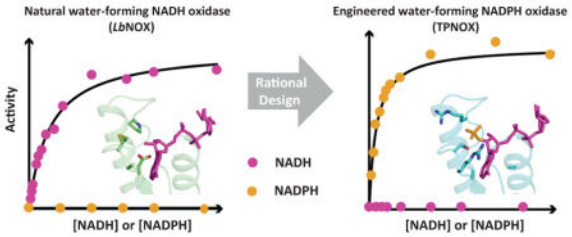

Introduction

All forms of life require unremitting flux of energy, which is achieved through complex redox chemistry performed at the cellular level. Two pyridine dinucleotides, NADH and NADPH, are essential in this process due to their ability to serve as electron carriers for a large subset of oxidoreductases. Despite the identical redox chemistry of NAD^+/NADH and $NADP^+$/NADPH redox couples, and, consequently, similar standard reduction potentials ($E^{o\prime} = -320$ mV), they work in their specific cellular environments at vastly different redox potentials (E_h), which are defined by the local concentrations of their oxidized and reduced forms. For example, in fed rat livers, the cytosolic free NAD^+/NADH ratio is about 1000, which corresponds to a reduction potential $E_h = -240$ mV, while the cytosolic free $NADP^+$/NADPH ratio is ~0.01, which is equivalent to the reduction potential $E_h \sim -400$ mV[1–4]. Cells maintain NADPH mostly in the reduced form to drive reductive biosynthesis and reactive oxygen species (ROS) detoxification, while the NADH pool is maintained mostly in the oxidized state to catalyze energy-producing reactions[4]. The preferential utilization of NADPH in anabolic processes and NADH in catabolic processes is an important design principle of cellular metabolism that allows thermodynamically incompatible reactions to take place simultaneously.

The diverse metabolic functions of NADH and NADPH are possible due to the specificity and varied distribution of cellular enzymes that utilize these coenzymes. Though NADPH differs from NADH only by the presence of a single phosphate group in the 2′ position of the adenosine ribose, most human enzymes have evolved to selectively use either one or the other. Equally important is the compartmentalized distribution of these enzymes. For example, mammalian mitochondria, whose membrane is not permeable to pyridine nucleotides, maintain the NAD^+/NADH pool in a more reduced state than in the cytosol. The difference is likely required to maintain thermodynamic favorability of oxidative phosphorylation in the mitochondria and glycolysis in the cytosol.

The activity of core metabolic pathways and shuttle systems help to establish the observed NAD^+/NADH and $NADP^+$/NADPH reduction potentials in different compartments[5]. The NAD^+/NADH ratio is determined by the relative activities of glycolysis in the cytosol, the tricarboxylic acid (TCA) cycle and electron transport chain (ETC) in mitochondria, as well as the activity of shuttle systems (e.g., aspartate–malate, glycerol-3-phosphate shuttles). The cytosolic $NADP^+$/NADPH reduction potential is determined primarily by the pentose phosphate pathway (PPP), cytosolic malic enzyme, isocitrate dehydrogenase, and one-carbon metabolism pathway. In mitochondria, NADPH can be produced by transhydrogenase, malic enzyme, isocitrate dehydrogenase, and the one-carbon metabolism

pathway. Furthermore, several shuttle systems for conversion of mitochondrial NADPH or NADH into cytosolic NADPH have been proposed[6,7]. Knockout studies indicate redundancy in NADPH producing pathways[5,8–10]. It is not well-understood which of these pathways maintain the $NADP^+$/NADPH reduction potential under different conditions.

There is growing evidence that the regulation of NAD^+/NADH and $NADP^+$/NADPH reduction potentials is extremely important in physiology and disease. These ratios are highly dynamic, changing depending on the fasting/fed state[1,2], diet[1,2,11], exercise[12], circadian rhythm[13], cell proliferation status[14] or pathologic states including cancer[14], diabetes[1] and the aging process itself[15,16]. There is also growing evidence that changes in pool sizes of pyridine nucleotides vary with disease processes[17]. To what extent these changes are reflective of underlying pathology versus drivers of pathology is not known.

To address these questions, robust methods are needed for measuring and manipulating pyridine nucleotide ratios in living cells. In recent years there has been progress in the development of genetic reporters for detecting the dynamics of NAD^+/NADH or $NADP^+$/NADPH in cells[18–21]. Mass spectrometry tracer methods for measuring fluxes through compartment specific NADH- and NADPH-producing pathways have also been developed[22–25]. However, methods for direct manipulation of NADH and NADPH levels in subcellular compartments are lacking.

We recently reported the use of NADH oxidase from *Lactobacillus brevis* (*Lb*NOX)[26] which catalyzes a four-electron reduction of oxygen to water ($2NADH + 2H^+ + O_2 \rightarrow 2NAD^+ + 2H_2O$) as a genetically encoded tool for manipulation of NAD^+/NADH ratios in human cells. Here we report the design and validation of TPNOX, a quintuple mutant of *Lb*NOX that is highly specific for NADPH. The X-ray structures of *Lb*NOX–NADH and TPNOX–NADPH complexes provide new insights into the substrate specificity of H_2O-forming oxidases. We show that TPNOX is active when expressed in mammalian cells and use it in combination with *Lb*NOX to demonstrate that intra-mitochondrial but not intra-cytosolic NADPH and NADH reduction potentials are connected.

Results

Rational design of the water-forming NADPH oxidase TPNOX

To our knowledge there are no naturally occurring H_2O-forming oxidases that are highly specific for NADPH ($2NADPH + 2H^+ + O_2 \rightarrow 2NADP^+ + 2H_2O$). Therefore, we sought to engineer an NADPH-specific mutant of the H_2O-forming oxidase from *L. brevis* (*Lb*NOX)[26]. Such an approach seemed feasible since several groups have had reasonable success in converting the NAD(P)H coenzyme specificities of various oxidoreductases[27].

The NADH binding site in *Lb*NOX and related enzymes contains two defined motifs: a conserved pyridine dinucleotide binding motif (DBM) GxGxxG/A, which is a part of the βαβ Rossmann fold domain, and an adjacent motif designated as “substrate specificity loop” (SSL) (Fig. 1a)[27]. Comparison of the amino acid sequence of *Lb*NOX with that of structurally related strictly NADPH-specific enzyme glutathione reductase (GR) and other related enzymes helped to identify five key residues spanning both motifs (numbered 1–5 in

Fig. 1a). Based on the structure of *Lb*NOX–NADH complex (determined in this study, see below) and the structure of GR-NADPH (PDB code 1GET) we rationalized that positions 2, 3 and 5 contribute to the GR preference for the phosphate-bearing NADPH over NADH (Fig. 1b,c; Supplementary Results, Supplementary Fig. 3a and Supplementary Table 1). The negatively charged side chain of Asp177 (position 2) stabilizes NADH binding in *Lb*NOX via two strong hydrogen bonds to the ribose hydroxyl groups in positions 2′ and 3′. To avoid charge repulsion with the phosphate moiety of NADPH, we replaced this residue with the neutral Ala, whose small side chain (rather than the larger Val197 found in GR) we considered less likely to interfere with the core residues of *Lb*NOX. As the phosphate group of NADPH in GR interacts directly with the positively charged side chains of Arg residues in positions 3 and 5 (Fig. 1b,c), we substituted both Ala178 and Pro184 in *Lb*NOX with arginine.

The contribution of the residue in position 4 to the substrate specificity in NOXes is uncertain. Dual-specificity NOXes from protozoan human parasite *Giardia intestinalis* and lactic bacterium *Lactobacillus sanfranciscensis*, which accept both NADH and NADPH but otherwise are very similar to *Lb*NOX, have His and Ser, respectively, at this position[28,29]. Both residues are capable of hydrogen bond formation with the 2′-phosphate group of NADPH. GR contains Lys at this position but surprisingly it does not interact with the substrate (Fig. 1c). Since the active site of the proposed variant already contains two positively charged arginines, we substituted the hydrophobic Met179 of *Lb*NOX with neutral Ser (rather than with positively charged His). It has been reported that mutations in the SSL that change the K_M for a specific substrate in expected manner often result in a drastic loss of catalytic activity (k_{cat}), an effect that can be alleviated by additional (usually random) mutations[27]. The substrate specificity of oxidases involves a still incompletely understood mechanism that signals the presence of the phosphate moiety at the adenosine end of NADPH (or the lack of it in NADH) to the distant redox site where the hydride ion transfer from the nicotinamide ring of NADPH to the isoalloxazine ring of FAD occurs[27]. In the case of GR, an important role in this putative mechanism appears to be played by the residue in the last position of the DBM motif (position 1, Fig. 1b,*c*) where Gly, which is preferred by NADH specific enzymes, is replaced with Ala[30,31]. Thus, we replaced Gly159 of *Lb*NOX with Ala. In total, we engineered a quintuple mutant of *Lb*NOX (G159A, D177A, A178R, M179S, P184R; Fig. 1a, Supplementary Fig. 1), which we named triphosphopyridine nucleotide oxidase (TPNOX), as triphosphopyridine nucleotide is the classical name for NADPH.

Kinetic analysis of TPNOX activity

We purified a histidine-tagged version of TPNOX and characterized its kinetic properties (Fig. 2a,b, Table 1, Supplementary Fig. 2). TPNOX was extremely reactive with NADPH (k_{cat} 307±68 s^{-1} and K_M 24±3 μM) and virtually non-reactive with NADH (k_{cat} 2.9±0.4 s^{-1} and K_M 264±45 μM), resulting in a final specificity for NADPH (defined as [$k_{cat}/K_{M(NADPH)}$]/[$k_{cat}/K_{M(NADH)}$]) of 1160±391-fold (Table 1). Most importantly, TPNOX was as catalytically potent with NADPH as the original enzyme *Lb*NOX with NADH. The later translated into the largest specificity change (defined as [final specificity$_{(TPNOX)}$]/[final specificity$_{(LbNOX)}$]) reported to date, (1.3±0.5)x10^8-fold (Table 1). Furthermore,

introduction of the five amino acid substitutions neither altered oligomerization state (tetramer in solution 186±3 kDa) nor changed H_2O_2 production (below 1% of the total amount of NADPH oxidized during the catalytic cycle) (Supplementary Fig. 2). The stoichiometry of NADPH to O_2 in the TPNOX-catalyzed reaction is equal to two, which agrees with a H_2O-forming NADPH oxidase reaction (Fig. 2b).

TPNOX enabled us to clarify some aspects of NAD(P)H specificity of NOXes, in particular the contributions of residues in positions 1 and 4 (Fig. 1b). Comparison of the kinetic parameters of TPNOX with three other *Lb*NOX variants (mutants 1–3, Table 1) offers interesting insights; all three variants contain Ala in position 2 and Arg in positions 3 and 5, but they preserve Gly in the DBM motif. A variant that retains the original Met in position 4 (mutant 1, Table 1) has a substantially increased K_M for NADH, as compared to wild-type *Lb*NOX, from 69±3 μM to 1135±329 μM, and preference for NADPH of 56±36-fold (Table 1). Substitution of Met179 with His (mutant 2) or Ser (mutant 3), the residues capable of hydrogen bond formation with the phosphate moiety of NADPH, causes a substantial decrease in K_M for NADPH, which is paralleled by a decrease in k_{cat}, leading to only a moderate (~9-fold) increase in catalytic efficiency. It appears that the hydrogen bond between the side chain of Ser179 (mutant 3) or His179 (mutant 2) and the phosphate group stabilizes the binding of both the substrate and the oxidized product, which leads to a decrease in k_{cat} if product dissociation is rate-limiting. Interestingly, changes in the catalytic activity of mutants 1–3 with respect to NADH follow a similar trend (Table 1), which suggests a possibility of a direct hydrogen bond interaction between the side chains of His179 or Ser179 and the ribose 2′ hydroxyl. These observations explain why there is little improvement in specificity despite a notable decrease in K_M among the three mutants we tested.

All variants where residues were mutated in positions 2–5 were active with NADPH but still accepted NADH as a substrate with a catalytic efficiency too high to be useful in cellular studies. The presence of Ala in place of Gly in the last position of the GxGxxG/A motif led to the highest k_{cat} with NADPH (307±68 s^{-1}) and lowest k_{cat} with NADH (2.9±0.4 s^{-1}), which together with respective changes in K_M, yield unprecedented increase in both final specificity and specificity change compared to the wild-type protein (Table 1).

Structural basis for the substrate specificity in TPNOX

The determinants of NAD(P)H recognition in the SSL (Fig. 1b,c), which directly affect the K_M for a coenzyme are relatively straightforward: binding is governed by the interaction preferences of the phosphate group in the 2′ position of the ribose ring[32]. In contrast, the mechanism of communication between this site and the catalytic site which impacts k_{cat} is far from clear[27]. To shed light on that mechanism, we determined the crystal structures of *Lb*NOX and TPNOX complexed with NADH and NADPH, respectively, and compared them to the structure of *Lb*NOX (PDB code 5ER0) (Fig. 3, Supplementary Tables 1–2, Supplementary Figs. 3–4). In substrate-free *Lb*NOX, the access to the isoalloxazine ring of FAD is blocked by the phenol rings of two Tyr residues (Tyr157 and Tyr186) (Fig. 3a). Only on their displacement (due to a transition to a different rotamer) can the nicotinamide ring of NADH come into proximity of FAD as required for hydride ion transfer (Fig. 3b). This

"two-tyrosine" switch of *Lb*NOX is distinct from the one previously described for GR[33,34], which involves only one Tyr residue structurally equivalent to Tyr157 of *Lb*NOX. The second tyrosine (Tyr186) of *Lb*NOX either supports Tyr157 in its blocking position in coenzyme-free *Lb*NOX structure or contributes to substrate binding via a hydrogen bond with the diphosphate moiety in the *Lb*NOX–NADH complex.

Comparison of the TPNOX–NADPH and *Lb*NOX–NADH complexes reveals subtle differences in the position and orientation of the adenosine ribose and of the diphosphate moieties (Fig. 3c,d). The ribose ring of NADPH is slightly rotated compared to that of NADH due to the absence of Asp177 in TPNOX, which in the *Lb*NOX–NADH structure forms strong hydrogen bonds with the ribose hydroxyls in 2′ and 3′ positions. The absence of Asp177 also allows rotation of Gly154, the first residue in the GxGYxG/A nucleotide binding motif, causing its carbonyl group to move away from the Ala159 side chain. The adenosine moiety of bound NADPH is positioned higher above the GxGYxA loop of the Rossman fold compared to NADH in the *Lb*NOX–NADH complex (Fig. 3c,d). The position of Tyr157, on the opposite side of the helix with respect to Ala159, is influenced by Gly154–Ala159 contact. Thus, we propose that the path of communication between the 2′ phosphate moiety of NADPH and the redox site involves the Gly154–Ala159 contact, which might facilitate displacement of Tyr157 side chain from its blocking position. The G159A mutation, specifically the Cβ atom of Ala159, appears to compensate for the rotation of Gly154 and the higher position of the ribose ring, which explains the critical role of this substitution in retaining the enzymatic activity of TPNOX compared to *Lb*NOX. The TPNOX–NADPH structure provides an explanation for the large decrease in K_M upon introduction of Ser in position 4. This residue makes a strong hydrogen bond to the phosphate oxygen atoms of NADPH. Unexpectedly, we found substantial differences in the conformation of the substrate binding loop among the four independently refined TPNOX monomers (Supplementary Fig. 4) suggesting flexibility of interaction with the substrate. However, due to fortuitous crystal lattice packing, in which the substrate binding loops of adjacent monomers abut each other, the interacting residues might be restricted in mobility and their ability to interact with the substrate in the crystal.

Together, the structural and enzyme kinetics data highlight the importance of the interplay between the SSL and the DBM. The D177A and G159A mutations change the backbone conformation of DBM, while the M179S mutation provide a hydrogen bond for the phosphate moiety of NADPH, an interaction further facilitated by the positive charge of Arg178 and possibly Arg184.

Expression and activity of TPNOX in human cells

We used lentiviral infection to generate HeLa cells expressing untargeted or mitochondria-targeted TPNOX (mitoTPNOX) under the control of doxycycline inducible promoter TRE3G. To compare the effects of TPNOX and *Lb*NOX side-by-side, we also generated HeLa cells that express *Lb*NOX and mito*Lb*NOX. TPNOX, mitoTPNOX, *Lb*NOX and mito*Lb*NOX were expressed at similar levels when induced with doxycycline (Fig. 4a). Expression of TPNOX or mitoTPNOX was well-tolerated, as cells appeared grossly normal

in morphology, and exhibited normal proliferative rates (see below). Cell fractionation demonstrated that the expressed proteins are properly localized in HeLa cells (Fig. 4b).

To determine whether the TPNOX expressed in human cells is enzymatically active, we took advantage of the fact that TPNOX consumes oxygen. Expression of TPNOX, mitoTPNOX, *Lb*NOX or mito*Lb*NOX increased oxygen consumption by 1.7, 2.6, 1.9 or 4.2-fold, respectively (Fig. 4c). The increase in oxygen consumption was resistant to antimycin, an inhibitor of complex III of the ETC, indicating that it is due to oxidase activity of TPNOX and not due to increase in ETC activity. Higher activity of mitoTPNOX compared to TPNOX is likely due to higher concentration of NADPH in mitochondria compared to cytosol, which is supported by fractionation experiments[35]. We note that it is important to take into account that in addition to oxidizing NADPH to $NADP^+$, TPNOX also consumes protons and oxygen and, therefore, could affect cellular pH or oxygen levels, depending on experimental context.

We also evaluated the effect of TPNOX and mitoTPNOX expression on whole cell $NADP^+$ and NADPH levels. Expression of mitoTPNOX led to a 1.5-fold increase in the whole-cell $NADP^+$/NADPH ratio, while expression of TPNOX did not have a significant effect (Fig. 4d). The effect of mitoTPNOX on the $NADP^+$/NADPH ratio is likely to be driven by changes in mitochondrial $NADP^+$ amounts because the whole-cell NADPH amount is in large excess compared to the whole-cell $NADP^+$ amount (Supplementary Fig. 6) and the majority of cellular $NADP^+$ resides within mitochondria[35].

Effects of TPNOX and *Lb*NOX on intermediary metabolism

We used GC-MS and flux measurements to characterize the effect of TPNOX, mitoTPNOX, *Lb*NOX and mito*Lb*NOX on cellular metabolism. First, we determined the effect of TPNOX, mitoTPNOX, *Lb*NOX and mito*Lb*NOX expression on intracellular metabolite levels using GC-MS (Supplementary Data Set 1). Out of 97 quantified metabolites, 24 changed significantly ($p < 0.05$, ANOVA followed by Tukey's posttest), including fourteen TCA cycle and PPP intermediates or related metabolites. TPNOX expression led to an increase in PPP intermediates while mitoTPNOX, *Lb*NOX or mito*Lb*NOX expression led to an increase in TCA cycle intermediates (Fig. 5a). To confirm that these metabolite changes lead to changes in corresponding pathway fluxes, we used $^{14}CO_2$ production from 1-^{14}C-glucose (produces $^{14}CO_2$ through the action of 6-phosphogluconate dehydrogenase (PGD)) and 1-^{14}C-glutamine (produces $^{14}CO_2$ through the action of alpha-ketoglutarate dehydrogenase (OGDH)) to measure PPP and TCA cycle fluxes, respectively. In agreement with GC-MS data, TPNOX increased PPP flux while mitoTPNOX, *Lb*NOX and mito*Lb*NOX increased TCA cycle flux (Fig. 5b,c). We observed no significant change in glucose consumption or lactate production, except for a small decrease of lactate secretion caused by *Lb*NOX (Fig. 5d,e). The latter effect is likely due to the increase of cytosolic NAD^+/NADH ratio caused by *Lb*NOX, which should lead to higher secretion of glycolytic pyruvate at the expense of lactate without affecting glucose uptake rate.

Mitochondrial NADH and NADPH pools are connected

Our observation that mitoTPNOX but not TPNOX led to activation of the TCA cycle prompted us to investigate the connection between compartment-specific NAD^+/NADH and $NADP^+$/NADPH reduction potentials. We observed that mitoTPNOX, *Lb*NOX or mito*Lb*NOX, but not TPNOX, increased the whole-cell NAD^+/NADH ratio (Fig. 5f, Supplementary Fig. 6). We interpret the changes in the whole-cell NAD^+/NADH ratio as reflective of changes in the mitochondrial NAD^+/NADH ratio because the changes are mostly due to NADH levels and most of the NADH inside the cell is localized to mitochondria[3,35,36]. In agreement with these results, mitoTPNOX, *Lb*NOX or mito*Lb*NOX, but not TPNOX, increased the levels of TCA cycle intermediates and flux through OGDH, a TCA cycle enzyme regulated by mitochondrial NAD^+/NADH (Fig. 5a,c). Our observation that mitoTPNOX expression can impact mitochondrial NAD^+/NADH ratio and TCA cycle flux shows that intra-mitochondrial NAD^+/NADH and $NADP^+$/NADPH reduction potentials are connected. It is noteworthy that mito*Lb*NOX expression did not cause an increase of the whole-cell $NADP^+$/NADPH ratio, indicating that mitochondrial NAD^+/NADH and $NADP^+$/NADPH reduction potentials are connected asymmetrically. That is, oxidation of $NADP^+$/NADPH leads to oxidation of NAD^+/NADH but not vice versa. The observation that *Lb*NOX but not TPNOX can increase the levels of pyruvate, TCA cycle intermediates, TCA cycle flux and NAD^+/NADH ratio (Fig. 5a,c,f) shows that cytosolic NAD^+/NADH and $NADP^+$/NADPH reduction potentials are not connected. This is further supported by the fact that TPNOX but not *Lb*NOX can increase the levels of PPP intermediates and PPP flux, which is allosterically regulated by the effect of $NADP^+$/NADPH ratio on the rate-limiting PPP enzyme glucose-6-phosphate dehydrogenase.

mitoTPNOX, but not TPNOX, complements an impaired ETC

Mammalian cells with a dysfunctional ETC cannot proliferate in the absence of uridine and pyruvate in cell culture media[37,38]. We previously used *Lb*NOX to formally demonstrate that pyruvate is required to stimulate NAD^+ regeneration and that expression of *Lb*NOX or mito*Lb*NOX can substitute for the pyruvate requirement[26]. Here, we tested whether TPNOX or mitoTPNOX can also rescue cell proliferation in the presence of Complex I inhibitor piericidin. Expression of mitoTPNOX but not TPNOX rescued pyruvate auxotrophy (Fig. 5g), thus supporting the conclusion that NAD^+/NADH and $NADP^+$/NADPH reduction potentials are connected in mitochondria but not in the cytosol. These results also suggest that under our experimental conditions in HeLa cells there is no shuttle system that would allow for rapid exchange between cytosolic NADPH and mitochondrial NADH, as has been described for some tissues[6].

Discussion

We have described the design and validation of TPNOX, a genetically encoded tool for compartment-specific manipulation of the $NADP^+$/NADPH ratio in living cells. We believe that this tool will complement *Lb*NOX by enabling the scientific community to study the regulation and physiological role of compartment-specific $NADP^+$/NADPH reduction potential changes in living cells.

Understanding NAD(P)H coenzyme specificity in oxidoreductases is an important and still not fully resolved problem in enzymology[27]. A major challenge in engineering NAD(P)H coenzyme specificity is that the phosphate group in the 2′ position of adenosine, which distinguishes NADPH from NADH, affects the kinetics of the enzyme despite the fact that it is distant from the chemically active nicotinamide ring, where the hydride ion transfer to the isoalloxazine moiety of FAD occurs. Despite multiple published examples of switching specificity outside of the two-dinucleotide-binding flavoprotein group of oxidoreductases, the full reversal of substrate specificity for an enzyme which is strictly specific for one coenzyme has not been reported[27]. In GR from *E. coli*, the NADPH-to-NADH switch resulted in modest final specificity (8.1-fold) and specificity change ($1.8x10^4$-fold)[30,39]. In a recent study, a H_2O-forming oxidase from *Streptococcus mutans* was used to create a panel of mutants with varying substrate specificity [40]. Although one of these variants had the same amino acids in positions 2, 3 and 5 as TPNOX, its final specificity for NADPH was only 10-fold[40]. To the best of our knowledge the only published examples of engineered enzymes with final specificity similar to that of *Lb*NOX and TPNOX are the amphibian *Rana perezi* alcohol dehydrogenase (ADH8) with 7600-fold $NADP^+$-to-NAD^+ switch and *Thermus thermophilus* isopropylmalate dehydrogenase (IMDH) with 1000-fold NAD^+-to-$NADP^+$ switch[41,42]. However, in both cases the wild-type enzyme is not strictly specific for one coenzyme. TPNOX from this study is as catalytically active with NADPH [$(1.2\pm0.3)x10^7$ s^{-1} M^{-1}] as the wild-type *Lb*NOX with NADH [$(9.3\pm0.5)x10^6$ s^{-1} M^{-1}] with final specificity of 1160±391-fold and specificity change of $(1.3\pm0.5)x10^8$-fold (Table 1). The highest $NADP^+$-to-NAD^+ specificity change reported previously was that of isocitrate dehydrogenase from *E. coli* ($1.4x10^6$-fold) and for NAD^+-to-$NADP^+$ change, that of IMDH from *T. thermophilus* ($8.7x10^4$-fold)[42,43].

Previously reported structures of NOXes, including *Lb*NOX, lacking NADH or NADPH coenzymes limited our ability to pinpoint the mechanism of substrate specificity in this group of enzymes[26,29,44]. Our results with *Lb*NOX and TPNOX bound to their respective substrates are generally consistent with previous findings on related enzymes, and substantially expand our understanding of the substrate specificity in NOXes (Fig. 3, Supplementary Figs. 3–4, Supplementary Tables 1–2). We confirmed the role of Tyr157 of *Lb*NOX; the structurally equivalent residues in GR from *E. coli* (Tyr197) or human (Tyr177) are biochemically and structurally well-characterized[33,34,45,46]. Upon NADPH binding this tyrosine swings out allowing access of nicotinamide moiety of NADPH to the isoalloxazine ring of FAD, in similar fashion to that of Tyr157 in *Lb*NOX–NADH or TPNOX–NADPH (Fig. 1a, Fig. 3a,b). The initial role of this tyrosine in GR as a simple “lid” on the NADPH-binding pocket and protection of reduced flavin during the catalytic cycle was subsequently dismissed[33,34]. It is clear, however, that Tyr157 and the nicotinamide ring mutually exclude each other from contacting FAD. We also observed a change in the position of Tyr186, which is a part of the SSL and which is not conserved in GR or other NOXes (Figs. 1a and 3a,b). Tyr186 supports Tyr157 in the blocking position in the absence of substrate and contributes to substrate binding by forming a hydrogen bond with the diphosphate moiety of NAD(P)H. Comparison of the *Lb*NOX–NADH and TPNOX–NADPH structures suggests a role for the Gly/Ala substitution in the last position of GxGYxG/A nucleotide binding motif in the remarkable NADH-to-NADPH change in specificity. Apparently, the contact between

Gly154 and G/A159 is of importance. In TPNOX, the G159A substitution compensates for the change in the position of the ribose ring of NADPH and restores the communication between the coenzyme binding site and Tyr157, which is important for catalysis (Fig. 3c,d).

Compartmentalization of redox reactions is one of the most important design principles of metabolism and can be achieved chemically (through the use of specific coenzymes), temporally (by performing reactions at distinct times), or physically (through deploying enzymes in specific subcellular compartments). Using *Lb*NOX, we previously showed in HeLa cells that oxidation of NADH within mitochondria leads to a secondary oxidation of cytosolic NADH, likely via shuttle systems[26]. Here, we used *Lb*NOX in combination with TPNOX to understand how cytosolic and mitochondrial NAD^+/NADH and $NADP^+$/NADPH pools are connected in HeLa cells. We provide evidence in living HeLa cells that mitochondrial NAD^+/NADH and $NADP^+$/NADPH pools are connected. Specifically, we found that expression of mitoTPNOX, like mito*Lb*NOX, can increase the whole-cell NAD^+/NADH ratio, can increase TCA cycle flux and levels of TCA cycle intermediates, and can rescue the proliferative defect in cells with inhibited ETC (Fig. 5a–g). It is known that mitochondria contain three classes of enzymes that in principle can mediate exchange of reducing equivalents between NADH and NADPH (Fig. 5h). First, transhydrogenase is a mitochondrial inner membrane enzyme that catalyzes transfer of hydride ion from NADH to $NADP^+$ while dissipating the proton motive force. Second, mitochondrial glutamate dehydrogenase can actually use either NADH or NADPH. Third, mitochondria contain several paralogous enzymes that use NADH or NADPH with high specificity to perform the same reaction. Metabolic tracing experiments that detect preferential deuterium label transfer from cytosolic NADH to mitochondrial NADPH over cytosolic NADPH are consistent with our results if we take into account the fact that malate–aspartate shuttle should transfer a deuterium label between cytosolic and mitochondrial NADH pools[24].

Our data indicate that cytosolic reducing equivalents do not rapidly exchange between NAD^+/NADH and $NADP^+$/NADPH. To the best of our knowledge, the cytosol does not contain enzymes that can use either NAD^+/NADH or $NADP^+$/NADPH to catalyze the same reaction. However, it has been proposed that cytosolic NAD^+- and $NADP^+$-dependent dehydrogenases are connected through one of the substrates and operate close to equilibrium (e.g. lactate dehydrogenase and malic enzyme)[47]. While *Lb*NOX rescues the proliferative defect in cells with an interrupted ETC, cytosolic TPNOX cannot (Fig. 5g). Moreover, TPNOX expression increases PPP flux and levels of PPP intermediates but does not impact the whole-cell NAD^+/NADH ratio or TCA cycle flux, suggesting that cytosolic NAD^+/NADH and $NADP^+$/NADPH reduction potentials are not connected. Our results are supported by metabolic tracing experiments that report no exchange of deuterium label between cytosolic NADPH and whole-cell NADH and preferential deuterium label transfer from cytosolic NADH to mitochondrial NADPH over cytosolic NADPH[24].

In HeLa cells, mitochondrial pyridine nucleotide pools are connected asymmetrically, where oxidation of mitochondrial NADPH causes oxidation of mitochondrial NADH but not vice versa. This conclusion is supported by similar observations achieved using indirect methods[48]. The mechanism of this asymmetry is currently unknown but could be the result of the activity of transhydrogenase in the mitochondria. Such asymmetry may be beneficial

to the cell since mitochondrial NAD^+/NADH ratios fluctuate depending on ATP demand and respiratory fuel availability, while $NADP^+$/NADPH reduction potential may need to remain stable to ensure adequate biosynthetic capacity and guard against oxidative stress.

Online Methods

Cell lines

HeLa cells were purchased from ATCC (CCL-2) and were cultured in DMEM without pyruvate (US Biological, D9802) supplemented with 3.7 g/l $NaHCO_3$, 10% dialyzed FBS (Life Technologies, 26400-044). Lentiviral-infected HeLa cells were cultured in DMEM without pyruvate (US Biological, D9802) supplemented with 3.7 g/l $NaHCO_3$, 10% dialyzed FBS (Life Technologies, 26400-044), 500 μg/ml geneticin (Life Technologies, 10131-035) and 10 μg/ml puromycin (Life Technologies, A1113803). All of the experiments were performed in the absence of geneticin and puromycin. Cells were regularly tested for mycoplasma and were mycoplasma free.

Plasmids and construction of different mutants

A synthetic TPNOX gene cloned into pUC57 vector was obtained from Genewiz (See Supplementary Fig. 1). TPNOX-encoding gene was digested with BamHI and XhoI and subcloned into a pET30a vector (Novagen). *Lb*NOX variants D177A/A178R/P184R, D177A/A178R/M179H/P184R and D177A/A178R/M179S/P184R were obtained using a Quickchange Lightning site-directed mutagenesis Kit (Agilent) using pET30a plasmid containing TPNOX sequence as a template and the following primers (only sense sequences are shown):

A159G: 5′-GGCGCCGGATACATCGGAGCCGAACTGGCCGAGGCC-3′

S179H: 5′-CTTCCTCATGACCCTAGCATGTCTGGCAATCAGGGT-3′

S179M: 5′-CGTCACCCTGATTGCCAGAATGGCTAGGGTCATGAG-3′

For expression in mammalian cells synthetic TPNOX and mitoTPNOX genes cloned into pUC57 vector were obtained from Genewiz (See Supplementary Fig. 1) and were subsequently subcloned into a pLVX-TRE3G vector (Clontech) using NotI and XhoI restriction cites.

Enzyme expression and purification

Recombinant TPNOX and other *Lb*NOX variants were expressed in One Shot BL21(DE3) competent *E. coli* cells (Thermo Fisher Scientific) and purified as described previously[26]. Proteins were immediately frozen in liquid nitrogen and stored at −80 °C until use. For all activity assays enzymes were cleaved with Enterokinase (EMD Millipore) to remove the N-terminal Hisx6 tag as described previously[26]. In crystallization experiments non-cleaved proteins were used.

Enzyme activity assays

Activity of enzymes with NAD(P)H (0.5–600 μM) was measured at 37°C by monitoring the decrease in absorbance at 340 nm in 50 mM NaPi, pH 7.5 buffer with 150 mM NaCl at 37°C

as described previously[26]. Each individual rate measurement was performed in duplicate or triplicate. Kinetic parameters reported are based on three individual experiments. The values of the kinetic parameters (K_M and V_{max}) were determined from fitting data with the Michaelis–Menten equation with SigmaPlot 13.0. Final specificity was calculated as [k_{cat}/$K_{M(NADPH)}$]/[k_{cat}/$K_{M(NADH)}$] and specificity change was calculated as [final specificity of *Lb*NOX variants]/[final specificity of wild-type *Lb*NOX][27]. To determine simultaneous oxygen and NADPH consumption a custom-built fluorimeter was used as described previously[26]. H_2O_2 production was monitored in a continuous assay based on the AmplexRed kit (Abcam) as described previously[26] (See Supplementary Fig. 2).

Crystallization and soaking experiments with NADH and NADPH

Initial screen to identify crystallization conditions for TPNOX was performed using a NanoTransfer NT8 pipetting robot and a Rock Maker for storage and imaging of trays (Formulatrix, MA). TPNOX (10 mg/ml in 10 mM HEPES, pH 7.5 buffer with 100 mM NaCl) was mixed with the mother liquor solutions (0.1 μl of protein solution and 0.1 μl of precipitant solution) from the MCSG Suite (Microlytic, MA) and incubated over a 50 μl reservoir in the sitting drop plates. Hanging drops (2 μl) were set up and equilibrated against 200 μl of reservoir solution to generate crystals for substrate soaking experiments for *Lb*NOX and TPNOX. Crystals were grown in 20 % PEG 3350, 0.2 M NH_4Cl for *Lb*NOX and in 25 % PEG 3350, 0.1 M Bis-Tris, pH 6.5, 0.2 M $(NH_4)_2SO_4$ for TPNOX at 21 °C. Crystals were briefly soaked for 1–3 min in the formulation with 15 % (v/v) of ethylene glycol supplemented with 20–30 mM NADH or NADPH and were quickly frozen in liquid nitrogen.

X-ray diffraction data, structure determination and refinement

X-ray diffraction data were collected at beamline 8.2.2 at the Advanced Light Source (Berkeley, CA). Data collected at λ=0.97 or 1.00 Å were indexed, integrated, and scaled using the software HKL-2000. PHENIX package was used to determine structures with molecular replacement using *Lb*NOX structure (PDB code 5ER0) as a model. Ligands were added at later stages of the refinement using Phenix.refine to eliminate bias and structure was edited with COOT. Refinement of the TPNOX-NADPH structure required correction for twinning (estimated twinned fraction ~37%). All figures depicting X-ray structures were generated using PyMol. Data collection and refinement statistics for both *Lb*NOX-NADH and TPNOX-NADPH are reported in Supplementary Tables 1–2. Ramachandran plot statistics for the *Lb*NOX-NADH structure, is as follows: favoured (96.84 %), allowed (3.16 %), outliers (0.00 %) and rotamer outliers (2.40 %). Statistics for the TPNOX-NADPH structure, is as follows: favoured (92.74 %), allowed (7.04 %), outliers (0.23 %) and rotamer outliers (4.95 %).

Lentivirus production

Half a million HEK293T cells were seeded per well in a 6-well plate (one plate per lentivirus) in 2 ml of High glucose DMEM (Life Technologies, 11995) with 10% FBS (Sigma, F2442). The next evening the medium was replaced with fresh DMEM and cells were transfected with 100 μl of transfection mixture per well. The transfection mixture contained 3 μl X-treme Gene 9 reagent (Roche, 06365787001), 500 ng psPAX2 (psPAX2

was a gift from Didier Trono, Addgene plasmid # 12260), 50 ng pMD2.G (pMD2.G was a gift from Didier Trono, Addgene plasmid # 12259), 500 ng of pLVX-Tet3G (Clontech) or pLVX-TRE3G-Luciferase (Clontech) or pLVX-TRE3G-*Lb*NOX or pLVX-TRE3G-mito*Lb*NOX or pLVX-TRE3G-TPNOX or pLVX-TRE3G-mitoTPNOX and Opti-MEM medium (Life Technologies, 31985-070) up to 100 μl. To make the transfection mixture, 50 μl solutions of X-treme Gene 9 and DNA mixtures were prepared separately and the DNA solution was added dropwise to the X-treme Gene 9 solution. The mixture was incubated at room temperature for 30 min before adding it to cells. Two days after transfection, medium was collected, centrifuged at 500 x *g* for 5 min to pellet cells and the supernatant was aliquoted and stored at −80 °C.

Generation of HeLa Tet3G Luciferase, *Lb*NOX, mito*Lb*NOX, TPNOX and mitoTPNOX cell lines

Hela Tet3G cells were produced first using lentivirus from pLVX-Tet3G (Clontech) vector and then HeLa Tet3G cells were infected with corresponding lentivirus from pLVX-TRE3G-Luciferase, *Lb*NOX, mito*Lb*NOX, TPNOX or mitoTPNOX to generate corresponding cell lines. Twenty thousand HeLa cells were seeded in 2 ml of DMEM without pyruvate (US Biological, D9802) supplemented with 3.7 g/l $NaHCO_3$, and 10% dialyzed FBS (Life Technologies, 26400-044) per well in a 6-well plate. Twenty-four hours after seeding, 2 ml of lentivirus solution (0.6 ml for Tet3G lentivirus) was added per well. Twenty-four hours after infection medium was replaced. After an additional twenty-four hours, medium was replaced with 2 ml of DMEM without pyruvate (US Biological, D9802) supplemented with 3.7 g/l $NaHCO_3$, 10% dialyzed FBS (Life Technologies, 26400-044), 500 μg/ml geneticin (Life Technologies, 10131-035) and 1 μg/ml puromycin (Life Technologies, A1113803). Cells were selected for one week, frozen and stored in liquid nitrogen. Cells were cultured in the presence of 500 μg/ml geneticin and 10 μg/ml puromycin and all the experiments were performed within a month after thawing fresh aliquot of cells.

Determination of cellular localization of expressed proteins

Localization of overexpressed *Lb*NOX, mito*Lb*NOX, TPNOX and mitoTPNOX was determined using cell fractionation experiments as previously described[26]. Protein levels were detected using western blot with antibodies for FLAG tag (Cell Signaling, cat. No. 2368, dilution 1:1000), LRPPRC (Sigma, cat. No. SAB2700419-100UL, dilution 1:1000), β-actin (Cell Signaling, cat. No. 8457S, dilution 1:1000) and ATP5A (Abcam, cat. No. ab14748, dilution 1:1000).

Oxygen consumption

Cells were seeded at 30–40 x 10^3 per well in XF24 24-well cell culture microplates in 200 μl of DMEM without pyruvate (US Biological, D9802) supplemented with 3.7 g/l $NaHCO_3$ and 10% dialyzed FBS (Life Technologies, 26400-044) and were incubated at 37 °C in 5% CO_2 incubator. Twenty-four hours later, 800 μl of media was added per well supplemented with doxycycline (final concentration – 300 ng/ml) or water. Twenty-four hours later, media was replaced with 950 μl of DMEM without pyruvate (US Biological, D9802) supplemented with 25 mM HEPES-KOH, pH 7.4 and 10% dialyzed FBS (Life Technologies, 26400-044) and OCR was measured using Seahorse XF24-3. Each measurement was performed over 4

min after a 2-min mix and a 2-min wait period. Basal measurements were collected 7 times and 2 measurements were collected after injection of antimycin (final concentration 1 μM). Measurements before and after addition of antimycin were averaged and normalized by the cell number.

GC-MS analysis of metabolites

Four million HeLa Tet3G Luciferase, *Lb*NOX, mito*Lb*NOX, TPNOX or mitoTPNOX cells were seeded per 15 cm dish in 25 ml of DMEM without pyruvate (US Biological, D9802) supplemented with 3.7 g/l $NaHCO_3$, 10% dialyzed FBS (Life Technologies, 26400-044). Twenty four hours later, media was exchanged to 25 ml of DMEM without pyruvate (US Biological, D9802) supplemented with 3.7 g/l $NaHCO_3$, 10% dialyzed FBS (Life Technologies, 26400-044) and 300 ng/ml doxycycline. Twenty four hours later, media was again exchanged to DMEM without pyruvate (US Biological, D9802) supplemented with 3.7 g/l $NaHCO_3$, 10% dialyzed FBS (Life Technologies, 26400-044) and 300 ng/ml doxycycline. Two hours later, media was aspirated, cell culture dish was placed on an ice-cold metal plate, cells were rinsed with 25 ml of ice-cold 0.9% NaCl for no more than 10 seconds, 5 ml of dry-ice cold 80% methanol was added, the plate was transferred to dry ice metal plate, cells were scraped with cell lifter for 30 sec and the lysate was transferred to 15 ml conical tube on dry ice. Thirty minutes later, cells were centrifuged at 1342 x g at 4 °C for 10 min. Supernatant was collected and stored on dry ice. The pellet was resuspended in 1 ml of 80% methanol on wet ice, vortexed for 10 sec, incubated for 15 min on wet ice and spun at 2000 x g for 5 min. The pellet was re-extracted one more time and all the supernatants were combined and stored at −80 °C overnight. Supernatants were evaporated using a Speedvac (without heating) and shipped to the Metabolomics Core Facility at the University of Utah on dry ice. Metabolomics analysis was performed at the Metabolomics Core Facility at the University of Utah which is supported by 1 S10 OD016232-01, 1 S10 OD021505-01 and 1 U54 DK110858-01. All GC-MS analysis was performed with an Agilent 7200 GC/Q-TOF fit with a CTC autosampler. Dried samples were suspended in 40 μL of 40 mg/mL O-methoxylamine hydrochloride (MOX) in pyridine and incubated for one hour at 30°C. Twenty five μL of this solution was added to autosampler vials and 40 μL of N-methyl-N-trimethylsilyltrifluoracetamide (MSTFA) was added automatically via the autosampler and incubated for 60 minutes at 37°C with shaking. After incubation 3 μL of a fatty acid methyl ester standard (FAMES) solution was added followed by a 1 μL injection into the gas chromatograph. The split mode with the inlet temperature was held at 250°C. A 10:1 split ratio was used for analysis. The gas chromatograph had an initial temperature of 95°C for one minute followed by a 40°C/min ramp to 110°C and a hold time of 2 minutes. This was followed by a second 5°C/min ramp to 250°C, a third ramp to 350°C, then a final hold time of 3 minutes. A 30-meter Phenomex ZB-5 MSi column with a 5-meter guard column was employed for chromatographic separation. Helium was used as the carrier gas at a rate of 1 mL/min. Due to the high amounts of several metabolites, the samples were analyzed once more at a tenfold dilution.

Determination of total NAD^+/NADH and $NADP^+$/NADPH ratios

Four hundred thousand HeLa Tet3G Luciferase, *Lb*NOX, mito*Lb*NOX, TPNOX or mitoTPNOX cells were seeded per 6 cm dish in 3 ml of DMEM without pyruvate (US

Biological, D9802) supplemented with 3.7 g/l $NaHCO_3$, 10% dialyzed FBS (Life Technologies, 26400-044). Twenty four hours later, media was exchanged to 3 ml of DMEM without pyruvate (US Biological, D9802) supplemented with 3.7 g/l $NaHCO_3$, 10% dialyzed FBS (Life Technologies, 26400-044) and 300 ng/ml doxycycline. Twenty four hours later, media was again exchanged to DMEM without pyruvate (US Biological, D9802) supplemented with 3.7 g/l $NaHCO_3$, 10% dialyzed FBS (Life Technologies, 26400-044) and 300 ng/ml doxycycline. Two hours later, media was aspirated, cell culture dish was placed on an ice-cold metal plate, cells were rinsed with 3 ml of ice-cold PBS for no more than 10 seconds, 0.5 ml of ice-cold 1:1 mixture of PBS and 1 % DTAB in 0.2 M NaOH was added, cells were scraped for 20 seconds and transferred to an ice-cold 1.5 ml centrifuge tube. Cell lysate was immediately divided into two 200 µl aliquots. One aliquot was left as is and the other aliquot was supplemented first with 2 µl of 1 M ascorbic acid and then with 100 µl of 0.4 M HCl with 10 mM ascorbic acid. Addition of ascorbic acid is essential for preventing chemical oxidation of NAD(P)H into $NAD(P)^+$ under low pH conditions, which can lead to overestimation of intracellular $NADP^+$ levels by several fold[49]. Both aliquots were heated at 60°C for 20 min to destroy reduced or oxidized nucleotides and NAD^+, NADH, $NADP^+$ and NADPH levels were determined using Promega NAD^+/NADH-Glo or $NADP^+$/NADPH-Glo kits using manufacturer's instructions (Catalog numbers, G9071 and G9081). Assay was validated by recovering known amounts of NAD^+, NADH, $NADP^+$ and NADPH that were added to cell lysate immediately after the addition of ice-cold 1:1 mixture of PBS and 1 % DTAB in 0.2 M NaOH.

PPP and TCA cycle activity

PPP and TCA cycle activity were estimated based on PGD and OGDH activity, which were determined by measuring $^{14}CO_2$ production from 1-^{14}C-glucose and 1-^{14}C-glutamine, respectively, based on a previously described method[50]. Fifteen thousand HeLa Tet3G Luciferase, *Lb*NOX, mito*Lb*NOX, TPNOX or mitoTPNOX cells were seeded per well of a 96-well plate in 0.2 ml of DMEM without pyruvate (US Biological, D9802) supplemented with 3.7 g/l $NaHCO_3$, 10% dialyzed FBS (Life Technologies, 26400-044). Three replicate wells were used for each condition and wells with cells were separated from each other by at least one empty well to minimize bleed-through. Twenty-four hours later, media was exchanged to 0.2 ml of DMEM without pyruvate (US Biological, D9802) supplemented with 3.7 g/l $NaHCO_3$, 10% dialyzed FBS (Life Technologies, 26400-044) and 300 ng/ml doxycycline. Twenty-four hours later, cells were washed twice with 0.2 ml of DMEM without pyruvate (US Biological, D9815-01) supplemented with 5 mM glucose, 4 mM (for PPP) or 1 mM (for TCA) glutamine, 5 mM sodium bicarbonate, 10 % dialyzed FBS, 25 mM HEPES (pH 7.4) and 300 ng/ml doxycycline and media was exchanged to 0.1 ml of the same medium supplemented with 5 µCi/ml 1-^{14}C-glucose or 2 µCi/ml 1-^{14}C-glutamine. Plates were covered with filter paper soaked in saturated $Ba(OH)_2$, sealed with parafilm and incubated in 37°C incubator for three (PPP) or two (TCA cycle) hours. Filter paper was washed with acetone, dried at room temperature overnight, circles corresponding to individual wells were cut out, placed in 1.5 ml centrifuge tubes with open lids and heated at 95°C for 15 min to dehydrate the filter paper. Amount of ^{14}C bound to filter paper associated with each well was quantified using scintillation counter. No detectable $^{14}CO_2$ production

was observed when 6-^{14}C-glucose was used instead of 1-^{14}C-glucose indicating that the majority of $^{14}CO_2$ produced from 1-^{14}C-glucose is derived from PPP.

Rescue of piericidin-induced inhibition of cell proliferation

Two thousand HeLa Tet3G Luciferase, *Lb*NOX, mito*Lb*NOX, TPNOX and mitoTPNOX cells were seeded in 200 µl of DMEM without pyruvate (US Biological, D9802) supplemented with 3.7 g/l $NaHCO_3$ and 10% dialyzed FBS (Life Technologies, 26400-044) per well in a black 96-well plate with a clear bottom (Corning, 3904). Twenty-four hours after seeding, 10 µl of 6 µg/ml doxycycline (300 ng/ml final concentration) or water was added to each well. Twenty-four hours after addition of doxycycline, medium was exchanged to DMEM without pyruvate (US Biological, D9802) supplemented with 3.7 g/l $NaHCO_3$, 10% dialyzed FBS (Life Technologies, 26400-044), ± 1 µM piericidin and ± 300 ng/ml doxycycline. After 0, 1, 2, 3 and 4 days after doxycycline addition, medium was aspirated and cells were fixed by adding 100 µl of 4% paraformaldehyde in PBS and incubating at room temperature for at least 30 min. Paraformaldehyde solution was aspirated and cells were stained with 200 µl of 1 µg/ml Hoechst 33345. Plates were covered with sealing aluminum foil and stored at 4 °C before counting cells in each well with Molecular Dynamics ImageXpress Ultra. Images of 96-well plates with fixed cells stained with Hoechst 33345 were collected using Molecular Devices ImageXpress Micro XLS. Four images were taken to cover the whole well. Images were analyzed and nuclei number per well was counted using CellProfiler 2.0 image analysis software[51,52]. The cell counting method had a linear range from 500 to 40000 cells per well as determined by counting plates with known number of cells seeded 6 hours prior to fixation.

Statistical analysis

Repeated measures ANOVA followed by Tukey’s multiple comparisons test was used to evaluate whether a significant difference exists between three or more groups of samples. ANOVA was justified as appropriate because the compared values are expected to be derived from a normal distribution and the variance is similar between the groups.

Supplementary Material

Refer to Web version on PubMed Central for supplementary material.

Acknowledgments

This work was supported by grants R01GM099683, R35GM122455 from the National Institutes of Health and by the Harvard Ludwig Center. This research used resources of the Advanced Light Source, which is a DOE Office of Science User Facility under contract no. DE-AC02-05CH11231. Metabolomics analysis was performed at the Metabolomics Core Facility at the University of Utah which is supported by 1 S10 OD016232-01, 1 S10 OD021505-01 and 1 U54 DK110858-01. VKM is an Investigator of the Howard Hughes Medical Institute.

References

1. Williamson DH, Lund P, Krebs HA. The redox state of free nicotinamide-adenine dinucleotide in the cytoplasm and mitochondria of rat liver. Biochem J. 1967; 103:514–27. [PubMed: 4291787]
2. Veech RL, Eggleston LV, Krebs HA. The redox state of free nicotinamide-adenine dinucleotide phosphate in the cytoplasm of rat liver. Biochem J. 1969; 115:609–19. [PubMed: 4391039]

3. Sies, H. Metabolic compartmentation. Academic Press; London ; New York: 1982.
4. Klingenberg M, Buecher T. Biological oxidations. Annu Rev Biochem. 1960; 29:669–708. [PubMed: 14409905]
5. Pollak N, Dolle C, Ziegler M. The power to reduce: pyridine nucleotides--small molecules with a multitude of functions. Biochem J. 2007; 402:205–18. [PubMed: 17295611]
6. MacDonald MJ. Feasibility of a mitochondrial pyruvate malate shuttle in pancreatic islets. Further implication of cytosolic NADPH in insulin secretion. J Biol Chem. 1995; 270:20051–8. [PubMed: 7650022]
7. Ronnebaum SM, et al. A pyruvate cycling pathway involving cytosolic NADP-dependent isocitrate dehydrogenase regulates glucose-stimulated insulin secretion. J Biol Chem. 2006; 281:30593–602. [PubMed: 16912049]
8. Freeman HC, Hugill A, Dear NT, Ashcroft FM, Cox RD. Deletion of nicotinamide nucleotide transhydrogenase: a new quantitive trait locus accounting for glucose intolerance in C57BL/6J mice. Diabetes. 2006; 55:2153–6. [PubMed: 16804088]
9. Pandolfi PP, et al. Targeted disruption of the housekeeping gene encoding glucose 6-phosphate dehydrogenase (G6PD): G6PD is dispensable for pentose synthesis but essential for defense against oxidative stress. EMBO J. 1995; 14:5209–15. [PubMed: 7489710]
10. Ducker GS, et al. Reversal of Cytosolic One-Carbon Flux Compensates for Loss of the Mitochondrial Folate Pathway. Cell Metab. 2016; 23:1140–53. [PubMed: 27211901]
11. Chen D, et al. Tissue-specific regulation of SIRT1 by calorie restriction. Genes Dev. 2008; 22:1753–7. [PubMed: 18550784]
12. Sahlin K, Katz A, Henriksson J. Redox state and lactate accumulation in human skeletal muscle during dynamic exercise. Biochem J. 1987; 245:551–6. [PubMed: 3663177]
13. O'Neill JS, Reddy AB. Circadian clocks in human red blood cells. Nature. 2011; 469:498–503. [PubMed: 21270888]
14. Schwartz JP, Passonneau JV, Johnson GS, Pastan I. The effect of growth conditions on NAD+ and NADH concentrations and the NAD+:NADH ratio in normal and transformed fibroblasts. J Biol Chem. 1974; 249:4138–43. [PubMed: 4369293]
15. Braidy N, et al. Age related changes in NAD+ metabolism oxidative stress and Sirt1 activity in wistar rats. PLoS One. 2011; 6:e19194. [PubMed: 21541336]
16. Zhu XH, Lu M, Lee BY, Ugurbil K, Chen W. In vivo NAD assay reveals the intracellular NAD contents and redox state in healthy human brain and their age dependences. Proc Natl Acad Sci U S A. 2015; 112:2876–81. [PubMed: 25730862]
17. Verdin E. NAD(+) in aging, metabolism, and neurodegeneration. Science. 2015; 350:1208–13. [PubMed: 26785480]
18. Zhao Y, et al. SoNar, a Highly Responsive NAD+/NADH Sensor, Allows High-Throughput Metabolic Screening of Anti-tumor Agents. Cell Metab. 2015; 21:777–89. [PubMed: 25955212]
19. Hung YP, Albeck JG, Tantama M, Yellen G. Imaging cytosolic NADH-NAD(+) redox state with a genetically encoded fluorescent biosensor. Cell Metab. 2011; 14:545–54. [PubMed: 21982714]
20. Cameron WD, et al. Apollo-NADP(+): a spectrally tunable family of genetically encoded sensors for NADP(+). Nat Methods. 2016; 13:352–8. [PubMed: 26878383]
21. Bilan DS, Belousov VV. Genetically encoded probes for NAD+/NADH monitoring. Free Radic Biol Med. 2016; 100:32–42. [PubMed: 27387770]
22. Fan J, et al. Quantitative flux analysis reveals folate-dependent NADPH production. Nature. 2014; 510:298–302. [PubMed: 24805240]
23. Liu L, et al. Malic enzyme tracers reveal hypoxia-induced switch in adipocyte NADPH pathway usage. Nat Chem Biol. 2016; 12:345–52. [PubMed: 26999781]
24. Lewis CA, et al. Tracing compartmentalized NADPH metabolism in the cytosol and mitochondria of mammalian cells. Mol Cell. 2014; 55:253–63. [PubMed: 24882210]
25. Jiang L, et al. Reductive carboxylation supports redox homeostasis during anchorage-independent growth. Nature. 2016; 532:255–8. [PubMed: 27049945]
26. Titov DV, et al. Complementation of mitochondrial electron transport chain by manipulation of the NAD+/NADH ratio. Science. 2016; 352:231–5. [PubMed: 27124460]

27. Cahn JK, et al. A General Tool for Engineering the NAD/NADP Cofactor Preference of Oxidoreductases. ACS Synth Biol. 2017; 6:326–333. [PubMed: 27648601]
28. Brown DM, Upcroft JA, Upcroft P. A H2O-producing NADH oxidase from the protozoan parasite Giardia duodenalis. Eur J Biochem. 1996; 241:155–61. [PubMed: 8898901]
29. Lountos GT, et al. The crystal structure of NAD(P)H oxidase from Lactobacillus sanfranciscensis: insights into the conversion of O2 into two water molecules by the flavoenzyme. Biochemistry. 2006; 45:9648–59. [PubMed: 16893166]
30. Scrutton NS, Berry A, Perham RN. Redesign of the coenzyme specificity of a dehydrogenase by protein engineering. Nature. 1990; 343:38–43. [PubMed: 2296288]
31. Hanukoglu I, Gutfinger T. cDNA sequence of adrenodoxin reductase. Identification of NADP-binding sites in oxidoreductases. Eur J Biochem. 1989; 180:479–84. [PubMed: 2924777]
32. Wallen JR, Paige C, Mallett TC, Karplus PA, Claiborne A. Pyridine nucleotide complexes with Bacillus anthracis coenzyme A-disulfide reductase: a structural analysis of dual NAD(P)H specificity. Biochemistry. 2008; 47:5182–93. [PubMed: 18399646]
33. Krauth-Siegel RL, Arscott LD, Schonleben-Janas A, Schirmer RH, Williams CH Jr. Role of active site tyrosine residues in catalysis by human glutathione reductase. Biochemistry. 1998; 37:13968–77. [PubMed: 9760231]
34. Berry A, Scrutton NS, Perham RN. Switching kinetic mechanism and putative proton donor by directed mutagenesis of glutathione reductase. Biochemistry. 1989; 28:1264–9. [PubMed: 2540822]
35. Tischler ME, Friedrichs D, Coll K, Williamson JR. Pyridine nucleotide distributions and enzyme mass action ratios in hepatocytes from fed and starved rats. Arch Biochem Biophys. 1977; 184:222–36. [PubMed: 21628]
36. Eng J, Lynch RM, Balaban RS. Nicotinamide adenine dinucleotide fluorescence spectroscopy and imaging of isolated cardiac myocytes. Biophys J. 1989; 55:621–30. [PubMed: 2720061]
37. Morais R, Gregoire M, Jeannotte L, Gravel D. Chick embryo cells rendered respiration-deficient by chloramphenicol and ethidium bromide are auxotrophic for pyrimidines. Biochem Biophys Res Commun. 1980; 94:71–7. [PubMed: 6248067]
38. King MP, Attardi G. Human cells lacking mtDNA: repopulation with exogenous mitochondria by complementation. Science. 1989; 246:500–3. [PubMed: 2814477]
39. Perham RN, Scrutton NS, Berry A. New enzymes for old: redesigning the coenzyme and substrate specificities of glutathione reductase. Bioessays. 1991; 13:515–25. [PubMed: 1755827]
40. Petschacher B, et al. Cofactor Specificity Engineering of Streptococcus mutans NADH Oxidase 2 for NAD(P)(+) Regeneration in Biocatalytic Oxidations. Comput Struct Biotechnol J. 2014; 9:e201402005. [PubMed: 24757503]
41. Rosell A, et al. Complete reversal of coenzyme specificity by concerted mutation of three consecutive residues in alcohol dehydrogenase. J Biol Chem. 2003; 278:40573–80. [PubMed: 12902331]
42. Chen R, Greer A, Dean AM. Redesigning secondary structure to invert coenzyme specificity in isopropylmalate dehydrogenase. Proc Natl Acad Sci U S A. 1996; 93:12171–6. [PubMed: 8901552]
43. Chen R, Greer A, Dean AM. A highly active decarboxylating dehydrogenase with rationally inverted coenzyme specificity. Proc Natl Acad Sci U S A. 1995; 92:11666–70. [PubMed: 8524825]
44. Wallen JR, et al. Structural Analysis of Streptococcus pyogenes NADH Oxidase: Conformational Dynamics Involved in Formation of the C(4a)-Peroxyflavin Intermediate. Biochemistry. 2015; 54:6815–29. [PubMed: 26506002]
45. Pai EF, Schulz GE. The catalytic mechanism of glutathione reductase as derived from x-ray diffraction analyses of reaction intermediates. J Biol Chem. 1983; 258:1752–7. [PubMed: 6822532]
46. Karplus PA, Schulz GE. Substrate binding and catalysis by glutathione reductase as derived from refined enzyme: substrate crystal structures at 2 A resolution. J Mol Biol. 1989; 210:163–80. [PubMed: 2585516]

47. Krebs HA, Veech RL. Equilibrium relations between pyridine nucleotides and adenine nucleotides and their roles in the regulation of metabolic processes. Adv Enzyme Regul. 1969; 7:397–413. [PubMed: 4391643]

48. Petcu LG, Plaut GW. NADP-specific isocitrate dehydrogenase in regulation of urea synthesis in rat hepatocytes. Biochem J. 1980; 190:581–92. [PubMed: 7470071]

49. Burch HB, Bradley ME, Lowry OH. The measurement of triphosphopyridine nucleotide and reduced triphosphopyridine nucleotide and the role of hemoglobin in producing erroneous triphosphopyridine nucleotide values. J Biol Chem. 1967; 242:4546–54. [PubMed: 4383634]

50. Tabor H, Tabor CW, Hafner EW. Convenient method for detecting 14CO2 in multiple samples: application to rapid screening for mutants. J Bacteriol. 1976; 128:485–6. [PubMed: 789350]

51. Carpenter AE, et al. CellProfiler: image analysis software for identifying and quantifying cell phenotypes. Genome Biol. 2006; 7:R100. [PubMed: 17076895]

52. Kamentsky L, et al. Improved structure, function and compatibility for CellProfiler: modular high-throughput image analysis software. Bioinformatics. 2011; 27:1179–80. [PubMed: 21349861]

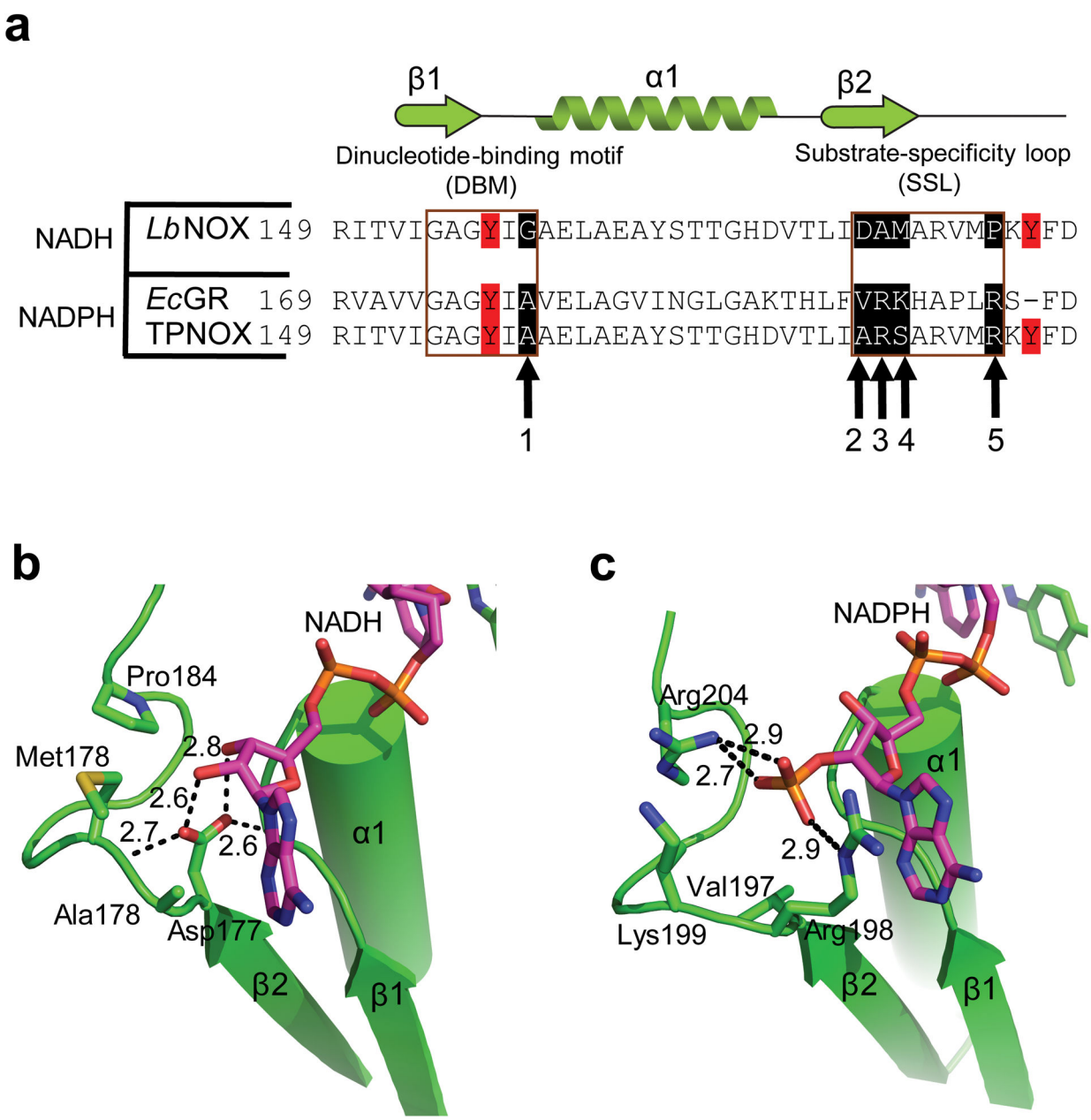

Figure 1. Engineering TPNOX, a water-forming NADPH oxidase

(**a**) Sequence alignment of the NAD(P)H-binding region of the Rossmann fold domain (βαβ) of H_2O-forming oxidase from *L. brevis* (*Lb*NOX), *E. coli* glutathione reductase (GR) and engineered TPNOX. Dinucleotide-binding motif (DBM) and substrate specificity loop (SSL) are boxed. Residues Tyr157 and Tyr186, which undergo large movements upon coenzyme binding are highlighted in red. (**b**,**c**) X-ray structures of *Lb*NOX–NADH (**b**, PDB code 5VN0) and GR–NADPH (**c**, PDB code 1GET) depicting the NAD(P)H-binding Rossmann fold domain. For clarity, alpha helix in both structures is shown as a cylinder. The measured distances are in Å.

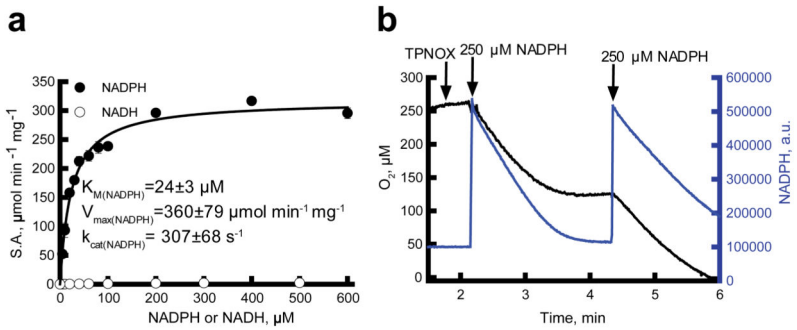

Figure 2. Catalytic activity of recombinant TPNOX

(**a**) The Michaelis–Menten analysis of the reaction catalyzed by TPNOX with NADPH or NADH. Inset shows kinetic parameters based on three independent experiments ± S.D. (**b**) Simultaneous measurements of oxygen and NADPH consumption by TPNOX. NADPH and enzyme were added as indicated by arrows.

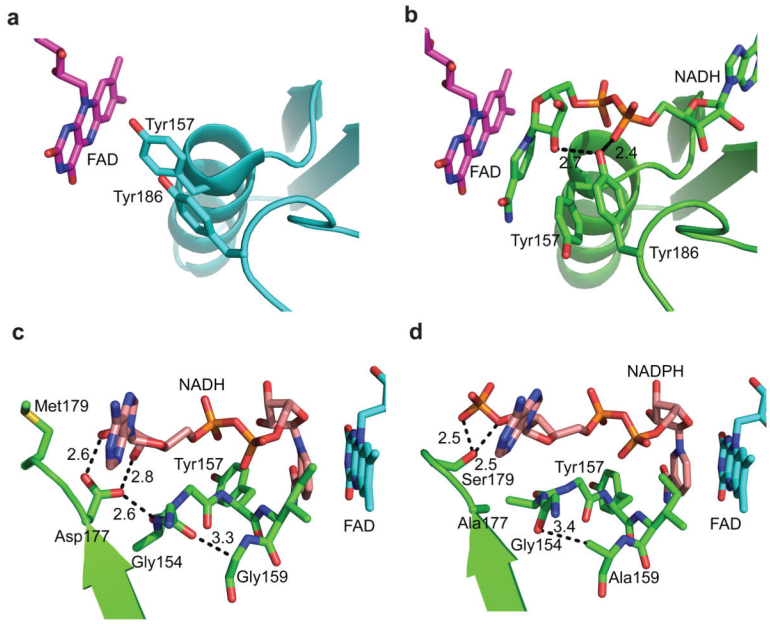

Figure 3. Structural determinants of NAD(P)H substrate selectivity in *Lb*NOX and TPNOX

(**a**,**b**) The "two-tyrosine" switch in *Lb*NOX. Comparison of the NADH binding site in coenzyme-free (**a**) and NADH-bound (**b**) *Lb*NOX structures (PDB codes 5ER0 and 5VN0, respectively). Note the transition from blocking to open position of Tyr157 and Tyr186 side chains. (**c**,**d**) The role of GxGxxG/A dinucleotide-binding motif (DBM) in NADH (**c**) and NADPH (**d**) recognition in *Lb*NOX and TPNOX (PDB codes 5VN0 and 5VOH, respectively). Note that Asp177 keeps the adenosine ribose ring of NADH in a tight contact with the GxGxxG motif (residues 154–159) due to the two strong hydrogen bonds with the 2′ and 3′ hydroxyl groups. In TPNOX, the ribose ring is rotated slightly and shifted upwards. The side chain of Ala159 in TPNOX compensates for rotation of Gly154 peptide bond and restores communication with the redox site.

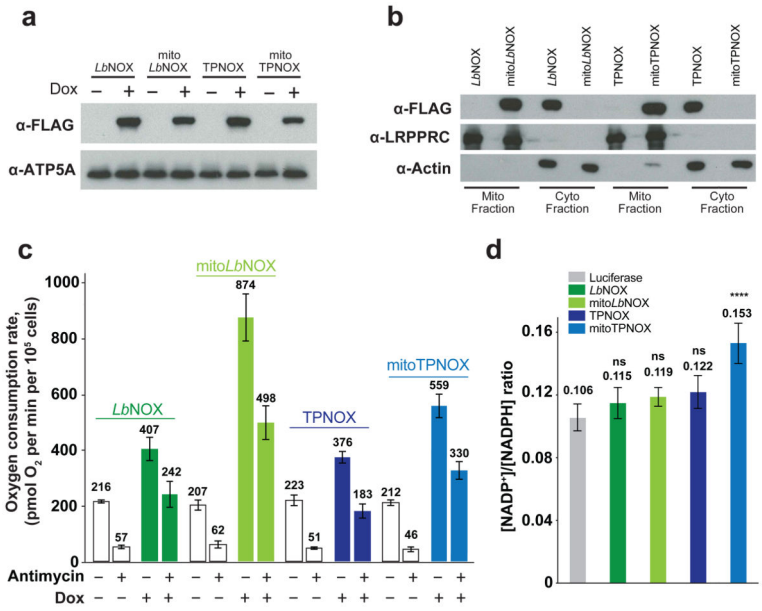

Figure 4. Expression and activity of TPNOX in human cells

(**a**) Western blot of TPNOX, mitoTPNOX, *Lb*NOX and mito*Lb*NOX expressed in HeLa cells 24-h after addition of doxycycline (Dox). (**b**) Subcellular localization of TPNOX, mitoTPNOX, *Lb*NOX and mito*Lb*NOX determined by cell fractionation. Full gel images for **a** and **b** are in Supplementary Figure 5. (**c**) Effect of *Lb*NOX, mito*Lb*NOX, TPNOX and mitoTPNOX expression on basal and antimycin-resistant (1 μM antimycin) oxygen consumption measured with Seahorse XF24 flux analyzer. Mean ± S.E.M. from n=3 independent experiments with five biological replicates in each experiment. (**d**) Effect of *Lb*NOX, mito*Lb*NOX, TPNOX and mitoTPNOX expression on total $NADP^+$/NADPH ratio. Mean ± S.E.M. from n=6 independent experiments with two biological replicates in each experiment. P-values were determined using repeated measures one-way ANOVA followed by Tukey's multiple comparisons test using GraphPad. ns, $p > 0.05$; ****, $p < 0.0001$.

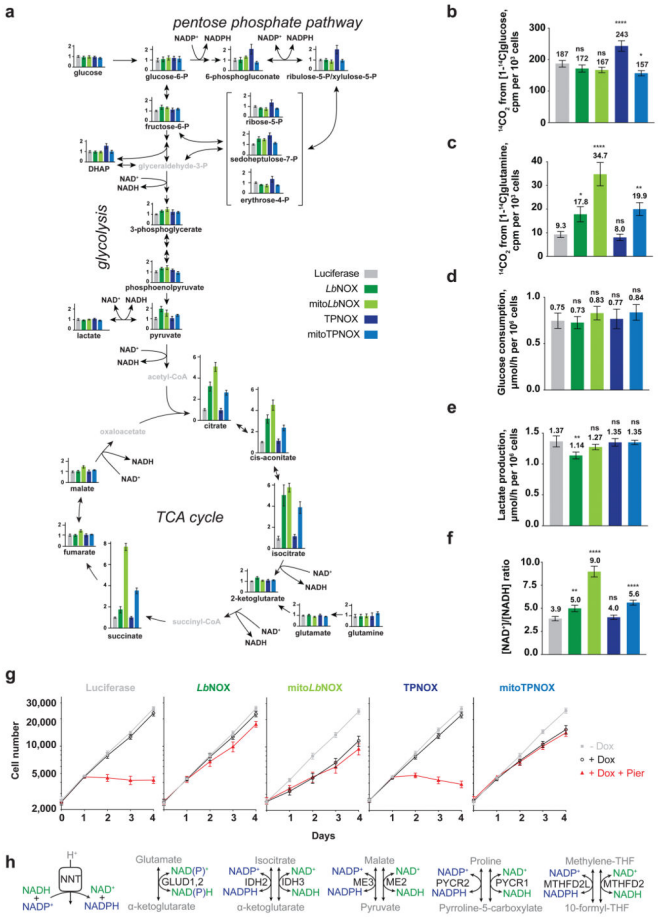

Figure 5. Metabolic consequences of compartment-specific perturbation of NADH or NADPH

Effects of overexpression of *Lb*NOX, mito*Lb*NOX, TPNOX, or mitoTPNOX on: (**a**) Intracellular metabolite levels determined by GC-MS. Adapted from Supplementary Data Set 1. Mean ± S.E.M. from n = 6 biological replicates; (**b**,**c**) Flux through 6-phophogluconate dehydrogenase (**b**) and 2-oxoglutarate dehydrogenase (**c**) as proxies for PPP and TCA cycle activities, respectively. Mean ± S.E.M. from n = 5 (**b**) and n = 4 (**c**) independent experiments with three biological replicates in each experiment; (**d**,**e**) Glucose consumption (**d**) and lactate production (**e**). Mean ± S.E.M. from n = 4 independent experiments with two biological replicates in each experiment; (**f**) Total [NAD^+]/[NADH] levels. Mean ± S.E.M. from n = 6 independent experiments with two biological replicates in each experiment; (**g**) Cell proliferation defect caused by 1 μM piericidin treatment on day 1. Mean ± S.E.M. from n = 4 independent experiments with six biological replicates per timepoint in each experiment. (**h**) Mitochondrial enzyme systems that may mediate the exchange between mitochondrial NAD^+/NADH and $NADP^+$/NADPH reduction potentials. P-values were determined using repeated measures one-way ANOVA followed by Tukey's multiple comparisons test using GraphPad. ns, $p > 0.05$; *, $p < 0.05$; **, $p < 0.01$; ****, $p < 0.0001$.

Table 1

Kinetic parameters of *Lb*NOX, TPNOX and *Lb*NOX variants

Activities were measured as described in Online Methods. Kinetic parameters represent the average of at least three independent experiments ± S.D. k_{cat} values were calculated per protein monomer using V_{max} values obtained in the Michaelis–Menten analysis.

Variant	Mutations					Substrate	K_M μM	k_{cat} s^{-1}	k_{cat}/K_M s^{-1} M^{-1}	Final Specificity for NADPH[a]	Specificity Change[b]
	DBM		SSL								
	159	177	178	179	184						
wt	G	D	A	M	P	NADH	69±3	648±28	$(9.3\pm0.5)\times10^{6}$		
*Lb*NOX						NADPH	621±124	0.052±0.001	$(8.3\pm1.6)\times10^{1}$	$(0.89\pm0.18)\times10^{-5}$	
Mut1	G	A	R	M	R	NADH	1135±329	59±18	$(5.2\pm2.1)\times10^{4}$		
						NADPH	61±20	178±67	$(2.9\pm1.4)\times10^{6}$	56±36	$(6.3\pm4.3)\times10^{6}$
Mut2	G	A	R	H	R	NADH	329±61	39±6	$(1.1\pm0.2)\times10^{5}$		
						NADPH	15±2	123±19	$(8.2\pm1.6)\times10^{6}$	69±21	$(7.7\pm2.9)\times10^{6}$
Mut3	G	A	R	S	R	NADH	18±3	7.9±1.0	$(4.3\pm0.9)\times10^{5}$		
						NADPH	2.8±0.5	76±12	$(2.7\pm0.6)\times10^{7}$	61±19	$(6.9\pm2.6)\times10^{6}$
TPNOX	A	A	R	S	R	NADH	264±45	2.9±0.4	$(1.1\pm0.2)\times10^{4}$		
						NADPH	24±3	307±68	$(1.2\pm0.3)\times10^{7}$	1160±391	$(1.3\pm0.5)\times10^{8}$

[a] Final specificity towards NADPH was calculated as $[k_{cat}/K_{M(NADPH)}]/[k_{cat}/K_{M(NADH)}]$ for each protein.

[b] Specificity change was calculated as [final specificity(*Lb*NOX variant or TPNOX)]/[final specificity(wild-type *Lb*NOX)][27]. DBM and SSL denote dinucleotide-binding motif and substrate specificity loop.